Available online at www.sciencedirect.com

SciVerse ScienceDirect

Journal of the European Ceramic Society 32 (2012) 1667–1680

www.elsevier.com/locate/jeurceramsoc

Crystallization of lead zirconate titanate without passing through pyrochlore by new solution process

Hiroyuki Kameda [a,b,*], Jinwang Li [a], Dam Hieu Chi [a,c], Ayumi Sugiyama [c], Koichi Higashimine [d], Tomoya Uruga [e], Hajime Tanida [e], Kazuo Kato [e], Toshihiko Kaneda [a], Takaaki Miyasako [a], Eisuke Tokumitsu [a,f], Tadaoki Mitani [a], Tatsuya Shimoda [a,g]

[a] *Japan Science and Technology Agency (JST), ERATO, Shimoda Nano-Liquid Process Project, 2-5-3 Asahidai, Nomi, Ishikawa 923-1211, Japan*
[b] *Electronic Materials Development Laboratory, ADEKA Corporation, 7-2-34 Higashi-ogu, Arakawa-ku, Tokyo 116-8553, Japan*
[c] *School of Knowledge Science, Japan Advanced Institute of Science and Technology, 1-1 Asahidai, Nomi, Ishikawa 923-1292, Japan*
[d] *Center for Nano Materials and Technology, Japan Advanced Institute of Science and Technology, 1-1 Asahidai, Nomi, Ishikawa 923-1292, Japan*
[e] *SPring-8, Japan Synchrotron Radiation Research Institute, 1-1-1 Koto, Sayo, Hyogo 679-5198, Japan*
[f] *Precision and Intelligence Laboratory, Tokyo Institute of Technology, 4259-R2-19 Nagatsuta, Midori-ku, Yokohama 226-8503, Japan*
[g] *School of Materials Science, Japan Advanced Institute of Science and Technology, 1-1 Asahidai, Nomi, Ishikawa 923-1292, Japan*

Received 7 September 2011; received in revised form 16 January 2012; accepted 18 January 2012
Available online 23 February 2012

Abstract

We report a novel low-temperature crystallization path for perovskite lead zirconate titanate (PZT) from solution. The modification of a PZT solution by monoethanolamine (MEA) resulted in a change in the crystallization behavior. MEA was strongly coordinated to the metal ions, resulting in destroy of multinuclear metal organic complexes. This led to a remarkably increased pyrolysis temperature, and Pb^{2+} was reduced into Pb^0 because of a reducing environment at 200–300 °C. Nanoscopic separations of Pb^0 was later transformed into uniformly distributed α-PbO nanocrystals and clusters in the amorphous Zr/Ti–O matrix, and finally the sample crystallized into perovskite at 400–500 °C. On the other hand, pyrochlore phase was observed in the conventional crystallization process. The avoidance of pyrochlore formation is the key for the low-temperature crystallization of perovskite. X-ray absorption fine structure (XAFS) analysis was performed to reveal the structures in solutions and amorphous phases.

Keywords: PZT; Precursor-chemical preparation; Electron microscopy; X-ray methods; Low-temperature crystallization

1. Introduction

Over the past 50 years a considerable number of studies about lead zirconate titanate ($PbZr_xTi_{1-x}O_3$, PZT) with perovskite structure (ABO_3) have been conducted. The reason for attracting a great interest is its multi-functional properties and wide applications such as pyroelectric sensors, piezoelectric actuators and non-volatile memories.[1,2] In general, PZT ceramics are prepared by a solid state reaction of Pb, Zr and Ti oxides at around 1200 °C, which often brings about microstructural and compositional heterogeneities due to huge grains (∼μm) of mechanically mixed reactants and high volatility of lead oxide at high temperatures (usually over 600 °C).[3] In addition, this technique is not applicable to the fabrication of thin (<300 nm) films.

In order to overcome these difficulties, the chemical solution process has been widely applied. In fact, solution processing is also considered the most important technique to solve environmental and energetical problems in the fabrication of advanced materials.[4] This process allows us to obtain fine grains and compositional homogeneity with no macroscopic phase separations, which enables lowering the sintering temperature of PZT.[5] Thin films have been fabricated by a simple spin-coating and annealing process, which has the advantages of low cost of both processing and facilities, easy control of film thickness, and readiness for large area deposition.

Unfortunately, the conventional chemical solution process has an inevitable disadvantage that it does not yield the desired perovskite phase directly. Pyrochlore phase ($A_2B_2O_{7-x}$), which

* Corresponding author at: Electronic Materials Development Laboratory, ADEKA Corporation, 7-2-34 Higashi-ogu, Arakawa-ku, Tokyo 116-8553, Japan. Tel.: +81 050 5518 4125; fax: +81 03 3809 8282.
E-mail address: kameda@adeka.co.jp (H. Kameda).

0955-2219/$ – see front matter © 2012 Elsevier Ltd. All rights reserved.
doi:10.1016/j.jeurceramsoc.2012.01.022

is known to be a metastable phase, appears after pyrolysis of metal organic compounds prior to the formation of perovskite. This is due to that pyrochlore phase is kinetically more favorable than the perovskite. The pyrochlore phase, which shows no ferroelectricity, has to be converted to the perovskite structure for ferroelectric and piezoelectric applications. Nevertheless, a high temperature (≥600 °C) is required for the structural change from pyrochlore to perovskite because a high energy barrier exists between them.[5–7] Such a high processing temperature raises severe issues when integrating with other parts because of significant interface diffusion and oxidation/degradation of other components (notably, silicon circuits), and consequently, leads to failure of the device.

In the present study, we have explored the crystallization behaviors of PZT solutions with the modification of alkanolamine with the aim of finding a low-temperature crystallization path for perovskite PZT. Alkanolamines, well-known additives for the solution process to make ceramics or thin films, were used as a chelating agent so far, which is commonly considered to increase the stability and solubility of metal organic compounds in a solution, resulting in compositional homogeneities of the system.[8–10] This compound was also adopted to the solution process of P(Z)T.[11–16] In recent results, Faheem and Shoaib succeeded in the fabrication of PZT nano-powders at 470 °C by the modification of triethanolamine to sol–gel system.[14] Further, Martin-Arbella et al. reported the solution process containing N-methyldiethanolamine using ultraviolet-assisted rapid thermal processing, and achieved crystallization of $PbTiO_3$ films at 400 °C.[15,16] These cases showed the low–temperature crystallization of perovskite by lowing the pyrolysis temperatures of the PZT precursors modified with alkanolamines.

Here we report, however, a new mechanism of low-temperature crystallization of PZT. Our modification with monoethanolamine (MEA), which is an alkanolamine, led to an increase in the pyrolysis temperature of PZT precursors. This is accompanied by compositional heterogeneities—a large amount of Pb^{2+} was reduced into Pb^0. We found that this heterogeneous condition enabled a skipping of pyrochlore formation, and the crystallization of perovskite occurred at low-temperatures (400–500 °C). Our finding is in contrast with previous studies that managed to avoid the reduction and separation of lead because this was thought to be unfavorable for crystallization.[17,18] In fact, according to the mechanism of our new path, we have succeeded in crystallization of high quality PZT films at low temperatures.[19]

We investigated in detail our finding of the new crystallization path of PZT, based on the observations of the crystallization behavior of powder samples from the two solutions with and without MEA modification, respectively. The results of powder X-ray diffraction (XRD), thermalgravimetric/differential thermal analysis (TG/DTA), transmission electron microscopy (TEM) combined with energy-disperse X-ray spectroscopy (EDS), X-ray photoelectron spectroscopy (XPS), and X-ray absorption fine structure (XAFS) analysis are presented. In particular, the structural difference between complexes in the two solutions was revealed by XAFS analysis. The difference was correlated to different behaviors in thermal decomposition and crystallization, giving explanation for reduction and separation of lead, and for the avoidance of pyrochlore formation, in samples with MEA. And then, re-oxidation accompanied by redistribution of lead from Pb^0 into PbO, and finally, conversion of PbO to PZT perovskite in MEA-modified samples were analyzed, with comparison to MEA-free samples.

2. Material and methods

2.1. Preparation of the PZT solutions

All chemicals were purchased from Kanto Chemical Co., Inc. (Tokyo, Japan) and used without further purification. The experiment was conducted in Ar gas to prevent hydrolysis of metal alkoxides. Two types of solution were prepared. The solution without MEA was named solution A, whereas the solution with MEA was named solution B. Pb acetate was selected as a Pb source by referring to the past report.[20] Zr and Ti n-butoxide were selected as Zr and Ti sources since they were commercially available and easy to handle. To fix a number of carbon chains among the metal organic compounds, n-butanol was adopted as the solvent.

The molar ratio of Pb, Zr, Ti, and MEA was fixed to be 1.0/0.4/0.6/2.0. Therefore, the number of MEA moles was equal to the total metal ions.

The solution samples were prepared as follows: a suspension of Pb acetate trihydrate (19.0 g = 50 mmol) in n-butanol (100 mL) was refluxed for 2 h, then water and by-products were completely removed as azeotrope. To the clear solution was added Zr n-butoxide (87% in n-butanol, 8.81 g = 20 mmol) and Ti n-butoxide (10.2 g = 30 mmol), and it was refluxed for another 2 h. This procedure produced solution A. Solution B was prepared by adding MEA (6.1 g = 100 mmol) to solution A, then further refluxing 2 h. The both solutions were pale yellow, and were adjusted by addition of n-butanol so that the total molar concentration of the metal ions became 1 mol/L.

2.2. Preparation of powder samples

Powder samples were prepared as follows: 2 g of solution A was divided and loaded into four 5-mL crucibles, and placed in the furnace under a dry air flow. A stepwise heating at an interval of 100 °C (first step at 200 °C) was scheduled, with a temperature rising time of 30 min between two steps and a holding duration of 1 h at each step. Samples finally heated at 200 °C, 300 °C, 400 °C, and 500 °C were named A200, A300, A400, and A500, respectively. Similarly, B200 to B500 were prepared from solution B at final temperatures of 200–500 °C.

The solvent molecules may coordinate to the metal organics. In order to clarify the structures of the samples after evaporation of the solvent but before heat treatment, two samples for XAFS analysis, named evaporated A and evaporated B, were prepared by removing the solvent from the solutions A and B, respectively, at 70 °C and under reduced pressure.

2.3. Characterization

XRD data were recorded with Cu-Kα radiation at 40 kV and 60 mA (model M18XHF-SRA, MacScience). Crystal sizes were estimated based on Scherrer's equation. TEM observations and selected-area electron diffraction (SAED) were performed on acceleration voltage of 300 kV (H9000NAR, Hitachi, Ltd.). TEM samples were prepared by dropping the suspension of powder in 2-propanol onto a Cu grid that was covered with a carbon thin film. EDS was also performed for elemental analysis. XPS (model PHI 5600, Physical Electronics) data were collected by using an Al-Kα monochrometer (ULVAC-PHI, Inc.), and data were calibrated using C 1s peak (284.8 eV). The depth analysis was carried out by Ar^+ ion etching at 2 keV.

XAFS measurements were conducted by using the beamline BL01B1 at SPring-8 (Japan). Pb L_3-edge (13,040 eV) and Zr K-edge (18,000 eV) XAFS spectra were measured in transmission mode. Ti K-edge (4965 eV) XAFS spectra were measured in fluorescence mode using a 19-element Ge detector. All measurements were performed at room temperature using a Si(1 1 1) double-crystal monochromator. The energy was calibrated with Cu foil. The powder samples were finely ground and diluted with BN, pressed into 1 mm thick pellets. Liquid samples were sealed in a transparent plastic bag through a handmade cell. The data analysis was performed using REX 2000.[21] Theoretical phase shifts and amplitude were calculated by FEFF 8.[22] Curve fitting for coordination distances such as Zr–Pb or Pb–Ti in the solution states were carried out by referring to the structural data in Refs. 23 and 24.

TG/DTA were carried out with TG/DTA6200 (SII NanoTechnology Inc.) from ambient temperature to 600 °C under an air flow and at a heating rate of 10 °C/min.

3. Results

3.1. X-ray diffraction

Fig. 1 shows the XRD results of A and B samples after the heat treatment at each temperature. For A samples, only a broad scattering peak was seen at around $2\theta = 30°$ after heating at 200 °C (A200). Further heating at 300 °C (A300) and 400 °C (A400) resulted in the peaks of Pb^0 fcc crystals at $2\theta = 31.3°$ and 36.3° (JCPDS: 4-686), with an average size of 53 nm estimated by Scherrer's equation. Finally, after heating at 500 °C (A500), Pb^0 peaks disappeared while strong but broad peaks were observed at $2\theta = 29.8°$ and 34.5°, which were attributed to the pyrochlore structure (JCPDS: 26-142) having a low crystallinity.

Significant differences compared with A samples were observed in the XRD patterns of B samples. Heating at 200 °C (B200) led to small but distinct peak of Pb^0 crystals in addition to the broad scattering peak. The formation of Pb^0 crystals was accelerated significantly by heat treatment at 300 °C (B300), which is lower than the melting point of Pb^0 (327.5 °C). The average size of the Pb^0 crystals in B300 was estimated to be 60 nm, which is slightly larger than that in A400. The height of peak intensities of Pb^0 crystals indicates that large quantity of Pb^0 phase existed in B300 compared to A400. In addition, a minor α-PbO crystals phase (JCPDS: 5-561) also appeared in B300. By heat treatment at 400 °C (B400), Pb^0 crystals disappeared, and α-PbO appeared as the major phase, of which the estimated crystal size was about 20 nm or less. By heat treatment at 500 °C (B500), well-crystallized perovskite was formed. In B samples, the pyrochlore phase was not observed in contrast to A samples.

3.2. TEM and XPS

In order to clarify the micro/nanostructure of phases and compositions, we conducted TEM and XPS measurements for B samples. Fig. 2 shows the TEM image of a typical particle in B300. Black areas of hundreds of nanometers in size can be seen in a gray matrix. SAED pattern of the gray matrix area exhibited halo rings from an amorphous phase (data not shown). In the black areas, however, SAED pattern was not obtained because of complete absorption of electron beams, so it indicates that many atoms of a heavy element (Pb) are condensed within that area.

Actually, EDS results showed a quite high amount of Pb existing in the black area compared with the gray matrix (Fig. 3). SAED performed with high-resolution TEM of the gray area

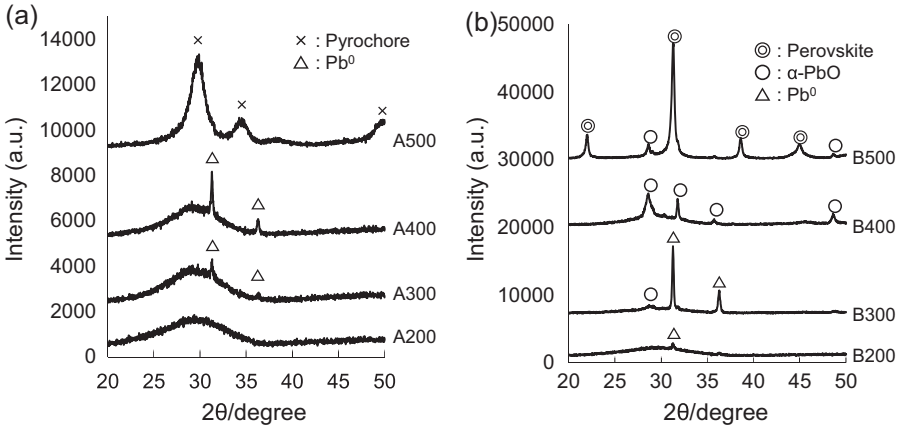

Fig. 1. X-ray diffraction patterns of PZT samples. (a) A samples (without MEA) and (b) B samples (with MEA).

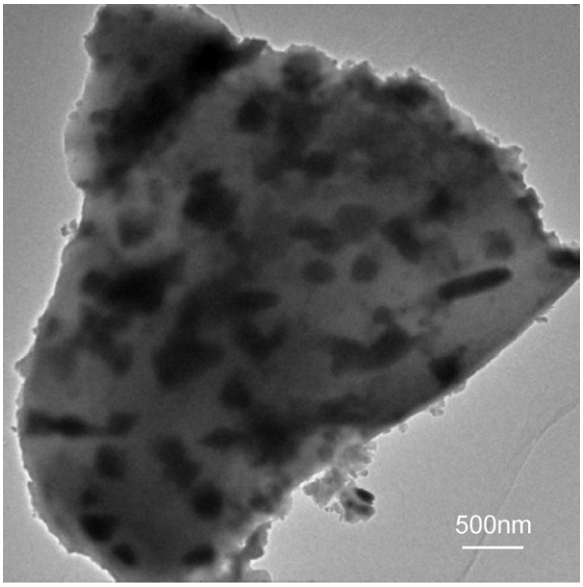

Fig. 2. TEM image of a typical particle in B300.

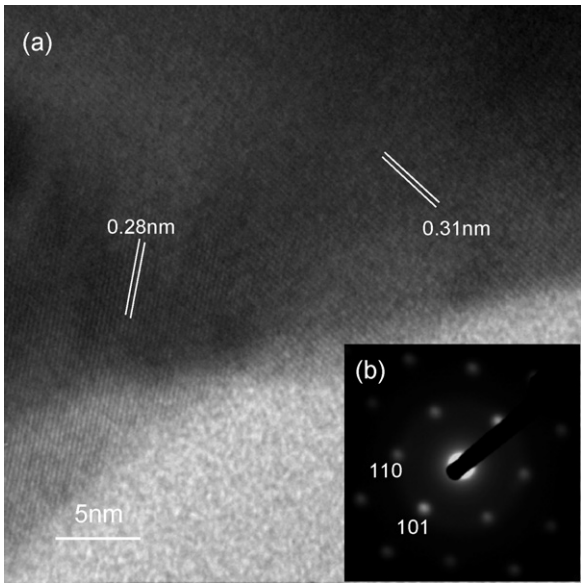

Fig. 4. (a) High-resolution TEM image in the gray area of B300 taken near the edge of the particle and (b) its SAED pattern, which are assigned to the α-PbO crystal.

near the edge of the particle showed the existence of α-PbO phase having high crystallinity (Fig. 4). Accordingly, the dominant component in the black area of B300 is Pb^0 crystal, while the gray area consists of amorphous compounds of Zr and Ti and a small amount of α-PbO crystal phase. The size of Pb^0 calculated from XRD data (60 nm) is much smaller than the size of the black areas (several hundreds of nanometers) in the TEM image, indicating these areas are agglomerated multicrystalline Pb^0.

To further confirm the valence states of Pb, XPS analysis was conducted (Fig. 5). The XPS spectrum from the surface of B300 powder showed divalence of Pb ($Pb4f_{7/2}$ at 138.8 eV and $Pb4f_{5/2}$ at 143.8 eV). After removing the surface by Ar^+ sputtering, the intensity of Pb^{2+} peaks decreased, while strong peaks at 137.0 eV and 141.9 eV, corresponding to Pb^0, appeared.[25] This result is consistent with the above TEM, EDS, and SAED analysis. It is reasonable that the inside of Pb^0 was protected against oxidation while the surface Pb was oxidized faster.

Fig. 6(a) shows a low resolution TEM image of B400. The clear contrast of the black and gray areas as was observed in B300 was not seen, indicating redistribution of Pb and a resulted much more uniform composition upon heating at 400 °C, which is higher than the melting point of Pb^0. The SAED pattern from the whole area (Fig. 6(b)) showed weak diffraction spots and broad Debye–Scherrer rings. The spots are assigned to large α-PbO nanocrystal which was estimated to be 20 nm in size from the XRD data, while the rings which coincide in angle with the diffraction spots of α-PbO and correspond to two broad risings ($2\theta = \sim 20–37^\circ$ and $\sim 42–62^\circ$, respectively) above the background in the XRD pattern (Fig. 6(c)), indicate the existence of α-PbO clusters. Thus, the separated and agglomerated Pb^0 in B300 was converted to uniformly distributed α-PbO nanocrystals and clusters in B400. Further it is quite important to point out the appearance of perovskite structure in B400. High-resolution TEM image and its SAED pattern in B400 (Fig. 7) give an

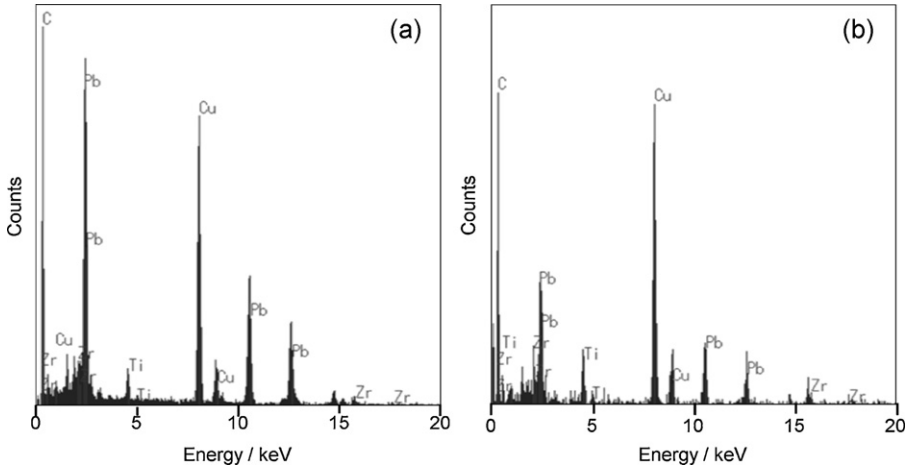

Fig. 3. EDS profiles of B300 (a) obtained from black area and (b) from gray area.

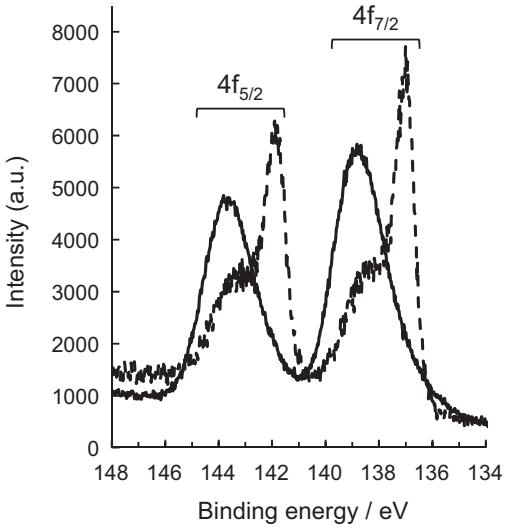

Fig. 5. XPS spectra of B300. Solid line: before sputtering; dot line: after sputtering.

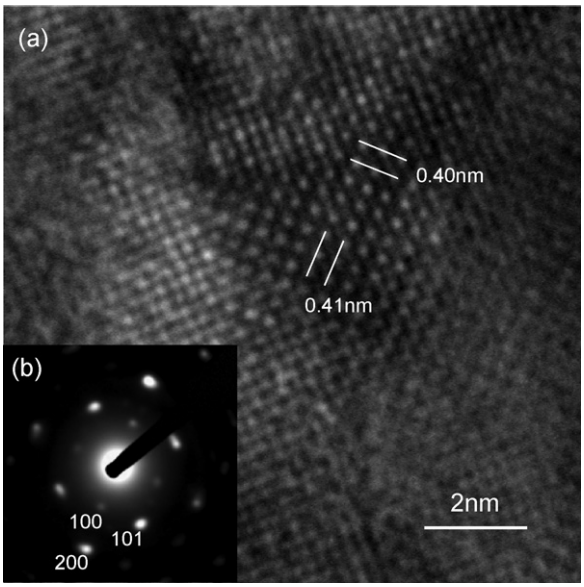

Fig. 7. (a) High-resolution TEM image of B400. (b) SAED patterns from (a), which are assigned to the perovskite crystal of PZT.

evidence of tetragonal unit cells in perovskite structure. This indicates that the heat treatment at 400 °C was high enough to start the crystallization of perovskite in B sample. XRD could not detect the perovskite in B400 because of the small amount.

3.3. XAFS

Our XRD and TEM observations gave only structural information about Pb in crystalline phase. We conducted XAFS analyses to examine the local structure and chemical state of Zr, Ti and Pb in solution and evaporated states, amorphous phase, and nano-crystalline phase. We compared the results of A and B samples to clarify effects of MEA on the local environment around metals.

3.3.1. Zr K-edge

Fig. 8 shows X-ray absorption near edge structure (XANES) spectra at Zr K-edge. The absorption edge energy measured indicates that Zr atoms in all the samples are Zr^{4+} species. In the spectra of both A and B samples, the main absorption peak

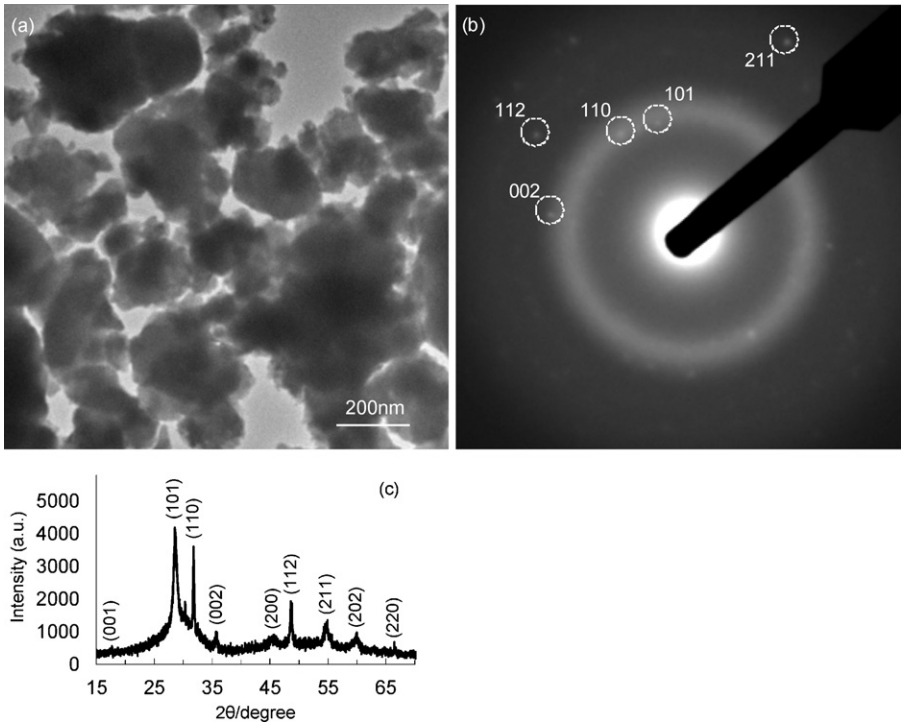

Fig. 6. (a) TEM image of B400 at low magnification, (b) SAED patterns from (a), and (c) XRD pattern of B400 with expanded intensities compared to that in Fig. 1. The indexed lines are from α-PbO nanocrystals, while the halo rings are from α-PbO clusters.

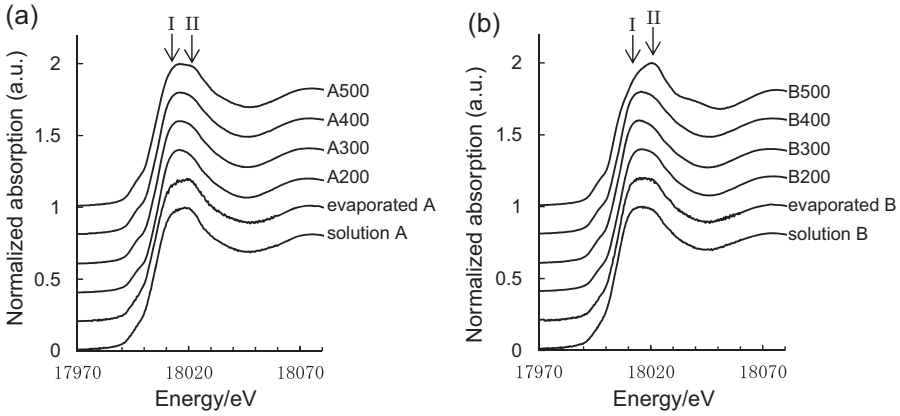

Fig. 8. Zr K-edge XANES spectra of PZT samples: (a) for A samples and (b) for B samples.

(white line peak) consists of two components at 18,016 eV and 18,021 eV, assigned as I and II, respectively.

The white line shape of solution A and evaporated A were dominated by component II similar to that of Zr n-propoxide, $Zr(OC_3H_7)_4$, having six fold coordination, while those of A200–400 exhibited a shift of major component from II to I which are similar to that of monoclinic ZrO_2 having seven fold coordination.[26] A500 showed a little increase of component II, which indicates the mixture of six and seven fold coordination.

On the other hand, for B samples, the white line shapes of solution B and evaporated B showed a major component (I) of seven fold coordination mixed with a component (II) of six fold coordination, whereas B200–400 showed only the seven fold line (I) of similar shape with that of ZrO_2. B500 clearly exhibited a major component II indicating six hold coordination in perovskite structure.[26]

Fig. 9 presents the observed and curve-fitted extended X-ray absorption fine structure (EXAFS) spectra (a) and their Fourier transforms (b) at Zr K-edge. The fitted parameters are listed in Table 1. In the solution state, both A and B samples showed Zr–O at the 1st neighbor (2.19, 2.29 Å) and Zr–Zr at the 2nd neighbor (3.36, 3.45 Å). These indicate the formation of multinuclear complexes. Oxygen atoms in alkoxides act as bridging ligand and form Zr–O–Zr linkage between adjacent metal atomes.[27] Zr–Zr distance at 3.45 Å in solution B was quite long compared with that in solution A (3.36 Å). This can be explained by larger steric hindrance between the Zr atoms in solution B because of MEA coordination. Also, the main coordination number was seven in solution B in contrast to six in solution A, as was seen in XANES data. In evaporated samples, further dissimilarity was found between A and B samples. Zr–Pb distance of 3.72 Å indicates that Zr–O–Pb structures appeared in evaporated A, while the spectrum of evaporated B did not exhibit such structure, and agreed with that of solution B. (Zr–O–Pb was not observed in the spectrum of solution A, perhaps because of coordination effect of the solvent molecules.) These results indicate that Zr–O–Pb linkage was destroyed by the addition of MEA in B samples. (See also the schematic image in Fig. 15.) Although MEA must have been coordinated to Zr atoms with hydroxyl or amine groups in its structure ($HO–C_2H_4–NH_2$) to form Zr–MEA complexes, the difference between Zr–O and Zr–N in the 1st neighbor could not be distinguished by the EXAFS data. The reason is probably that the atomic radii of nitrogen and oxygen were quite similar.

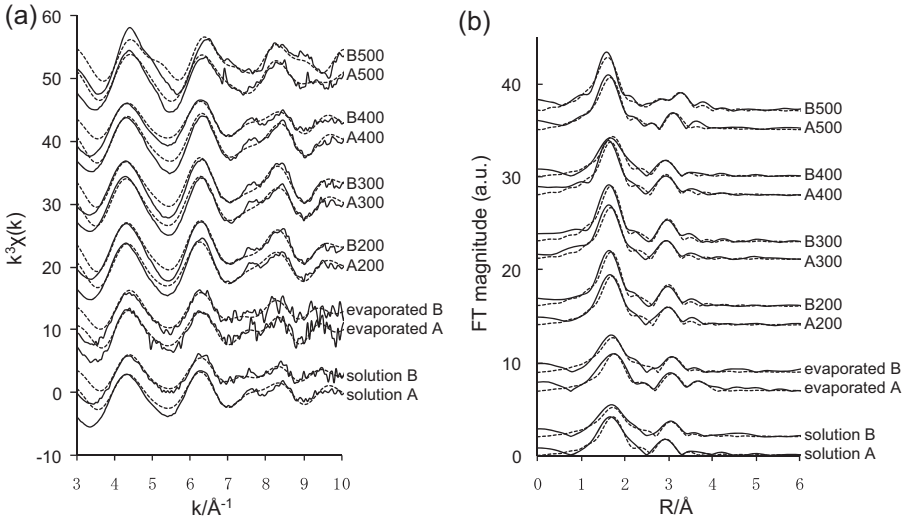

Fig. 9. Zr K-edge EXAFS spectra of PZT samples: (a) $k^3\chi(k)$ functions and (b) Fourier transforms of (a). Experimental (solid line) and calculated (dotted line).

Table 1
Fitting results of PZT samples from Zr K-edge EXAFS.

	Zr neighbor[a]	R[b] (Å)	N[c]	(σ^2)[d]	R-Factor (%)	k-Range (Å^{-1})
Solution A	O	2.19 (1)	4.0 (3)	0.010[e]	3.9	3–12
	Zr	3.36 (4)	1.8 (4)	0.010[e]		
Evaporated A	O	2.21 (2)	3.7 (3)	0.010[e]	2.8	3–12
	Zr	3.42 (6)	1.4 (5)	0.010[e]		
	Pb	3.72 (5)	2.6 (10)	0.010[e]		
A200	O	2.18 (1)	5.0 (4)	0.010[e]	3.1	3–12
	Zr	3.41 (4)	1.9 (5)	0.010 (21)		
A300	O	2.17 (1)	5.4 (10)	0.009 (1)	3.7	3–12
	Zr	3.38 (4)	2.1 (6)	0.010 (5)		
A400	O	2.16 (2)	4.7 (8)	0.009 (1)	4.6	3–12
	Zr	3.37 (4)	2.1 (5)	0.010[e]		
A500	O	2.14 (2)	4.7 (4)	0.010[e]	2.3	3–12
	Zr	3.53 (5)	1.8 (6)	0.010[e]		
Solution B	O	2.29 (2)	3.8 (9)	0.014 (1)	3.0	3–12
	Zr	3.45 (4)	1.6 (4)	0.010 (2)		
Evaporated B	O	2.19 (2)	4.5 (9)	0.014 (1)	3.5	3–12
	Zr	3.49 (4)	1.7 (4)	0.010 (2)		
B200	O	2.17 (2)	4.5 (8)	0.009 (1)	4.2	3–12
	Zr	3.42 (4)	2.2 (6)	0.010 (6)		
B300	O	2.16 (1)	5.2 (9)	0.009 (1)	2.6	3–12
	Zr	3.41 (4)	2.5 (6)	0.010 (3)		
B400	O	2.19 (1)	4.1 (3)	0.010[e]	4.4	3–12
	Zr	3.36 (4)	1.8 (4)	0.010[e]		
B500	O	2.10 (2)	5.3 (10)	0.011 (1)	3.7	3–12
	Pb	3.27 (5)	2.8 (12)	0.010[e]		
	Zr	3.80 (4)	4.0 (11)	0.010[e]		

Uncertainty of the last figure is given in parentheses.
[a] Backscatterers.
[b] Atomic distance.
[c] Coordination number.
[d] Debye-Waller factor.
[e] Fixed parameter.

After the heat treatment at 200 °C, the above differences between evaporated A and evaporated B disappeared in A200 and B200, and both samples exhibited almost the same EXAFS spectra with evaporated B. In addition, there are no significant differences in the EXAFS spectra between A200–400 and B200–400, as well as in the XANES spectra, indicating the same local structure and chemical states of Zr with local structures similar to monoclinic ZrO_2. Further, the XRD data did not show crystalline peaks originated from Zr compounds, so that Zr-oxides in all the A and B samples heated at 200–400 °C were in the amorphous states. It is obvious that these Zr atoms have the different local structure from those of the perovskite phase.[28]

EXAFS spectra of A500 and B500 show the features of the pyrochlore and perovskite structure. In B500, the observed coordination distances of Zr–Pb at 3.27 Å and of Zr–Zr at 3.80 Å correspond to those of B–A site and B–B site in the perovskite structure.

3.3.2. Ti K-edge

Fig. 10 shows XANES spectra of A and B samples at Ti K-edge. Unfortunately, good-quality XANES and EXAFS spectra of solution A and solution B could not be obtained due to very weak fluorescent X-rays of Ti atoms as a result of strong absorption by surrounding solvent and heavy elements.

It is well-known that pre-edge peaks at the Ti K-edge are strongly influenced by the symmetry of metal center. All of the samples prepared showed the weak peaks I at 4968 eV, which indicates the six-fold and octahedral coordination for Ti neighbors.[29] B500 showed weaker peaks II at 4971 eV, which is the sign of the existence of Zr around Ti atom in perovskite structures.[30]

The white line profiles of evaporated A and evaporated B were similar with Ti alkoxides,[31] and profiles of A500 and B500 were identical with that of pyrochlore and perovskite structure, respectively.[30,32] It is evident that the white line shapes

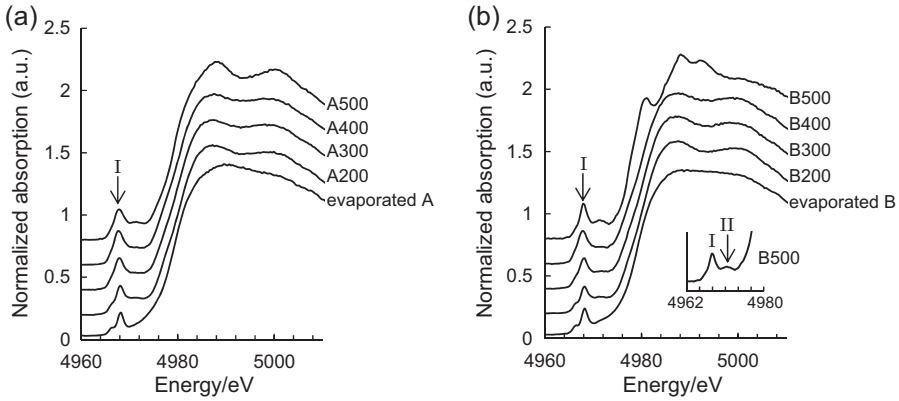

Fig. 10. Ti K-edge XANES spectra of PZT samples: (a) for A samples and (b) for B samples.

of A200–400 and B200–400 showed almost the same features, and indicated the similar local structure to anatase TiO_2.

Fig. 11 shows EXAFS spectra (a) and their Fourier transforms (b) at Ti K-edge. The fitted parameters are listed in Table 2. Clear difference was not confirmed in evaporated A and evaporated B for the low qualities of data. On the other hand, after heating at 200 °C, the same EXAFS spectra were found in A200 and B200. Ti–O at the 1st neighbor (1.96, 1.98 Å) and Ti–Ti at the 2nd neighbor (3.05 Å, 3.05 Å) indicate the formation of multinuclear complexes and Ti–O–Ti structures. The reason why Ti–Pb at over 3 Å was not observed is due to very weak fluorescence X-rays of Ti atoms. In addition, A200–400 and B200–400 showed identical EXAFS spectra, which means that Ti formed the same local environment as anatase TiO_2.[28] Further, since a crystalline phase of Ti was not observed in XRD data, the formation of amorphous TiO_2 was suggested. These Ti atoms have a different local structure with those in the perovskite phase, as in the case of Zr.

The EXAFS spectra of A500 showed the features of the pyrochlore structure, and B500 displayed perovskite structure which had the coordination distances at 1.98 Å for Ti–O, 3.30 Å for Ti–Pb and 4.13 Å for Ti–Ti.

3.3.3. *Pb L_3-edge*

Figs. 12 and 13 show XANES and EXAFS spectra at Pb L_3-edge of A and B samples. XANES spectra showed that the major parts of all the samples were close to the Pb^{2+} state. The fitted parameters of EXAFS spectra are listed in Table 3. The evaporated samples could not produce suitable absorption edge jump because of concentrated heavy atoms. The EXAFS oscillations at Pb L_3-edge in the large k-region were too small to give reliable information from the 2nd neighbor coordination. According to the past report, Pb L_3-edge EXAFS spectra cannot give correct information concerning Pb–Pb coordination in Pb^0 crystal, because of large fluctuations of their bonding.[33] So, we describe qualitatively the local structure around Pb atoms in this section.

In the solution states of A and B samples, Pb–O at the 1st neighbor (2.29, 2.21 Å) and Pb–Ti at the 2nd neighbor (3.42, 3.47 Å) indicate the existence of multinuclear complexes involving Pb–O–Ti linkage. In solution B, however, the coordination distance (2.21 Å) at the 1st neighbor was shorter and peak intensity at the 2nd neighbor was smaller, than those of solution A. These can be explained by the collapse of bridge structures between Pb and Ti because of the addition of MEA, as well as

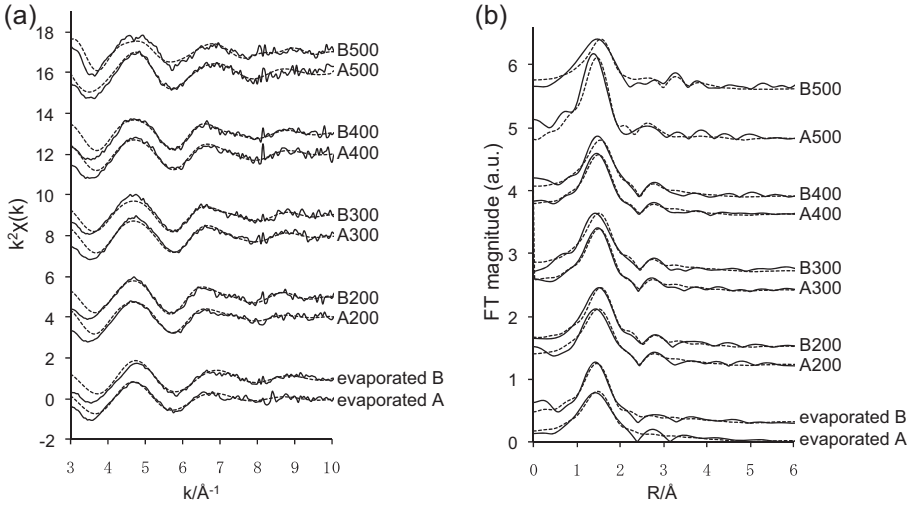

Fig. 11. Ti K-edge EXAFS spectra of PZT samples: (a) $k^2\chi(k)$ functions and (b) Fourier transforms of (a). Experimental (solid line) and calculated (dotted line).

Table 2
Fitting results of PZT samples from Ti K-edge EXAFS.

	Ti neighbor[a]	R[b] (Å)	N[c]	(σ^2)[d]	R-Factor (%)	k-Range (Å^{-1})
Evaporated A	O	1.95 (2)	3.3 (9)	0.014 (1)	2.4	3–10
A200	O	1.96 (2)	4.1 (11)	0.014 (1)	1.8	3–10
	Ti	3.05 (15)	0.7 (4)	0.010[e]		
A300	O	1.96 (2)	3.6 (8)	0.010 (1)	0.6	3–10
	Ti	3.01 (18)	0.6 (4)	0.010 (25)		
A400	O	1.96 (2)	3.6 (8)	0.011 (1)	0.6	3–10
	Ti	3.04 (18)	0.5 (4)	0.010[e]		
A500	O	1.94 (2)	2.9 (5)	0.007 (1)	3.4	2–10
	Ti	3.14 (16)	0.7 (5)	0.010 (65)		
Evaporated B	O	1.93 (2)	3.2 (6)	0.009 (1)	1.5	3–10
B200	O	1.98 (2)	3.3 (9)	0.009 (2)	0.7	3–10
	Ti	3.05 (11)	0.6 (7)	0.004 (42)		
B300	O	1.95 (2)	3.7 (10)	0.011 (1)	3.5	3–11
	Ti	3.03 (9)	0.4 (5)	0.003 (39)		
B400	O	1.97 (2)	3.7 (10)	0.012 (1)	1.7	3–11
	Ti	3.04 (10)	0.6 (7)	0.006 (27)		
B500	O	1.98 (2)	2.9 (7)	0.011 (1)	10.6	3–12
	Pb	3.30 (7)	1.7 (9)	0.010[e]		
	Ti	4.13 (25)	0.6 (8)	0.010[e]		

Uncertainty of the last figure is given in parentheses.
[a] Backscatterers.
[b] Atomic distance.
[c] Coordination number.
[d] Debye-Waller factor.
[e] Fixed parameter.

by the increase in a number of terminal alkoxides which have a shorter Pb–O distance than bridge ones. Unfortunately, the difference between Pb–N and Pb–O in the 1st neighbor could not be distinguished either, for the same reason mentioned for the EXAFS data of Zr.

After heating at 200 °C, however, the difference of EXAFS spectrum between A200 and B200 disappeared, and Pb–O distance became the same in both samples. The coordination number of Pb–Ti at the 2nd neighbor was smaller than one in the solution states. Moreover, Pb–Pb distance could not be found, either. These indicate that the collapse of multinuclear structures was accelerated, so that Pb compounds with smaller size mainly existed.[34]

After further heating, although A300–400 showed similar fitted results with A200, the coordination number of Pb–O in B300 significantly decreased. The absorption edge in XANES spectrum slightly shifted to lower energy compared with B200. These results are consisted with the formation of Pb^0 observed by XRD. Unfortunately, Pb–Pb distance (3.5 Å) could not be observed, as described above.[33] The structure of α-PbO observed in the XRD and TEM data was not seen in the EXAFS spectra, because of their small amount.

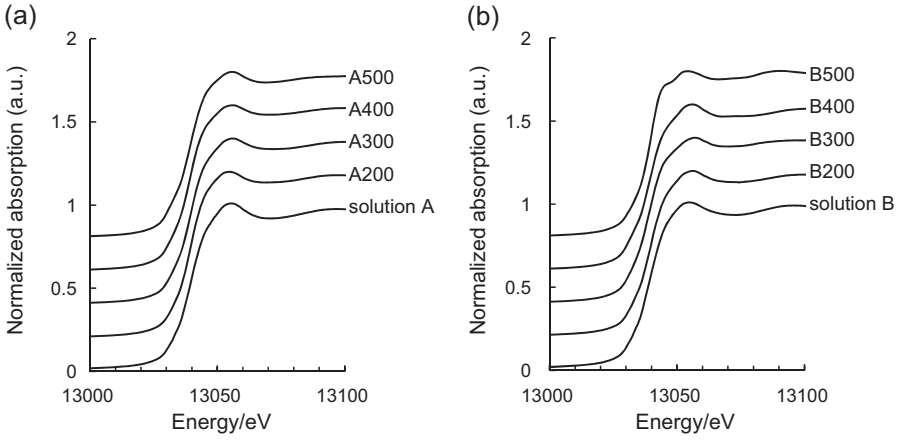

Fig. 12. Pb L_3-edge XANES spectra of PZT samples: (a) for A samples, (b) for B samples.

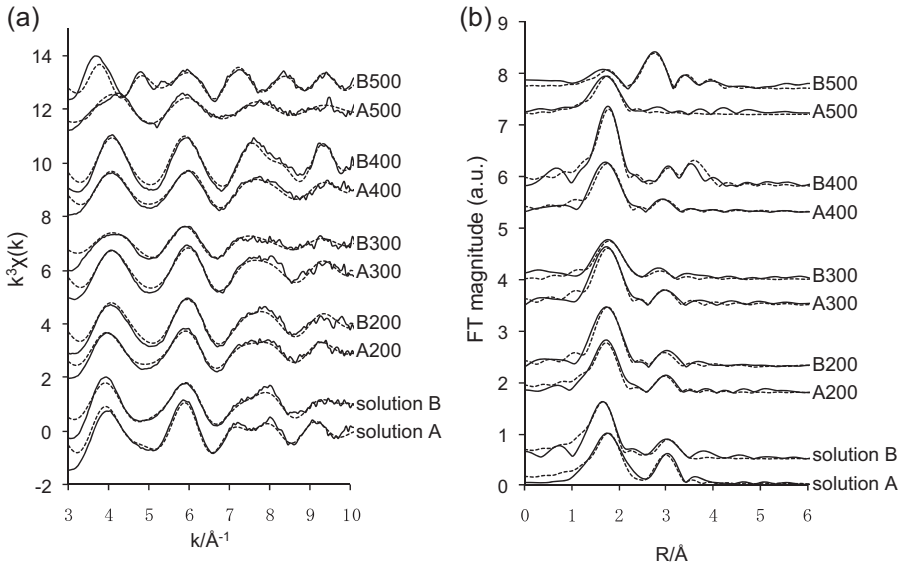

Fig. 13. Pb L_3-edge EXAFS spectra of PZT samples: (a) $k^3\chi(k)$ functions and (b) Fourier transforms of (a). Experimental (solid line) and calculated (dotted line).

Table 3
Fitting results of PZT samples from Pb L_3-edge EXAFS.

	Pb neighbor[a]	R[b] (Å)	N[c]	(σ^2)[d]	R-Factor (%)	k-Range (Å^{-1})
Solution A	O	2.29 (2)	1.9 (4)	0.013 (1)	10.7	3–12
	Ti	3.42 (3)	0.8 (1)	0.010[e]		
A200	O	2.25 (2)	1.3 (2)	0.001 (1)	6.0	3–12
	Ti	3.39 (4)	0.2 (2)	0.005 (7)		
A300	O	2.27 (2)	1.3 (3)	0.008 (1)	4.2	3–10
	Ti	3.35 (9)	0.2 (3)	0.004 (38)		
A400	O	2.27 (2)	1.1 (2)	0.008 (1)	4.0	3–10
	Ti	3.35 (9)	0.3 (1)	0.010[e]		
A500	O	2.27 (1)	0.9 (1)	0.010[e]	8.8	2.55–11
Solution B	O	2.21 (2)	1.6 (3)	0.011 (1)	3.2	3–12
	Ti	3.47 (4)	0.5 (1)	0.010[e]		
B200	O	2.28 (2)	1.4 (2)	0.011 (1)	8.5	3–12
	Ti	3.45 (5)	0.4 (3)	0.010 (5)		
B300	O	2.31 (2)	0.9 (1)	0.010[e]	8.0	3–12
	Ti	3.36 (5)	0.1 (1)	0.005 (7)		
B400	O	2.26 (2)	1.7 (3)	0.008 (1)	4.3	3–12
	Ti	3.39 (7)	0.4 (5)	0.010 (10)		
	Pb	3.69 (4)	1.6 (4)	0.010 (4)		
B500	O	2.32 (3)	0.5 (1)	0.010 (4)	2.4	3–12
	O	3.02 (2)	1.8 (2)	0.010 (8)		
	Ti	3.74 (4)	0.5 (1)	0.010 (13)		

Uncertainty of the last figure is given in parentheses.
[a] Backscatterers.
[b] Atomic distance.
[c] Coordination number.
[d] Debye-Waller factor.
[e] Fixed parameter.

In B400, the Pb–Pb coordination distance was observed at 3.69 Å, which corresponds to Pb–Pb separation in α-PbO crystal structure.[35] The fitted results indicated that α-PbO was the major phase in B400, which is consistent with the TEM observations. The minor perovskite component observed in the high-resolution TEM image (Fig. 7) could not be detected in the present EAXFS spectra, because of their small amount. In addition, a small coordination number of Pb–Ti indicates formation of an amorphous Pb–Ti/Zr–O phase.

In B500, the atomic distances at 3.02 Å and 3.74 Å could be identified as Pb–O and Pb–Ti coordination corresponding to the perovskite structure. Another Pb–O distance at 2.32 Å is attributed to that of α-PbO, indicating a small amount of α-PbO remained. In contrast, A500 showed no features of perovskite structure, in consistent with the XRD spectrum showing pyrochlore of low crystallinity.

3.4. Thermal analysis

Fig. 14 shows TG/DTA curves of A and B samples. In Fig. 14(a), A200 exhibits two distinct exothermic peaks in the DTA curve (dot line) at around 300 and 470 °C. The weight of A200 gradually decreased with heating up to 320 °C and was kept at almost constant during heating between 320 and 470 °C as is seen in the TG curve (solid line). This observation indicates that the pyrolysis of metal organic compounds had been completed at around 320 °C. A300 and A400 did not show the first DTA peak nor a weight loss below 320 °C, because heating at 300 °C for 1 h was sufficient to remove the organics. The weight of A200 slightly increased at 470 °C, and subsequently decreased again up to 600 °C. The similar phenomenon around 470 °C was observed in A300 and A400 (see Fig. 14(a) inlet). These suggest that oxygen deficient pyrochlore ($A_2B_2O_{7-x}$) absorbed some oxygen atoms and crystallized into composition of less oxygen deficiency (smaller x). The XPS analysis of A400 showed only a C 1s peak originated from carbon, and no peaks were found corresponding to the metal organic compounds (data not shown). Therefore, it should be considered that the weight decrease in the range of 470–600 °C was due to the release of the residual carbon and excess oxygen arising from the transformation from pyrochlore ($A_2B_2O_7$) to perovskite (ABO_3).[6,36] (XRD analysis revealed that A500 was converted to the perovskite phase after heated in 600 °C). It is supposed that carbon was formed by the pyrolysis of the metal organic compounds below 320 °C in A200, which conducted a partial reduction of Pb^{2+} to Pb^0 metal ($2PbO + C \rightarrow 2Pb + CO_2$).[37] No weight change from 320–470 °C suggests that the amount of Pb^0 formed between 320 °C and 400 °C was quite small, which is consistent with the XRD results of A400.

In Fig. 14(b), in contrast to A samples, a large weight loss of B200 (−28% at 600 °C) was estimated, which was about twice of those of A200 (−15% at 600 °C), whereas drastic changes in DTA were not observed before showing a very high exothermic peak at 450 °C. This result suggests that MEA strongly coordinated to the metal ions, affecting the pyrolysis behavior of B samples.

For B300, the DTA curve showed two broad exothermic peaks with gradual decrease of weight. The phase separated Pb^0 might

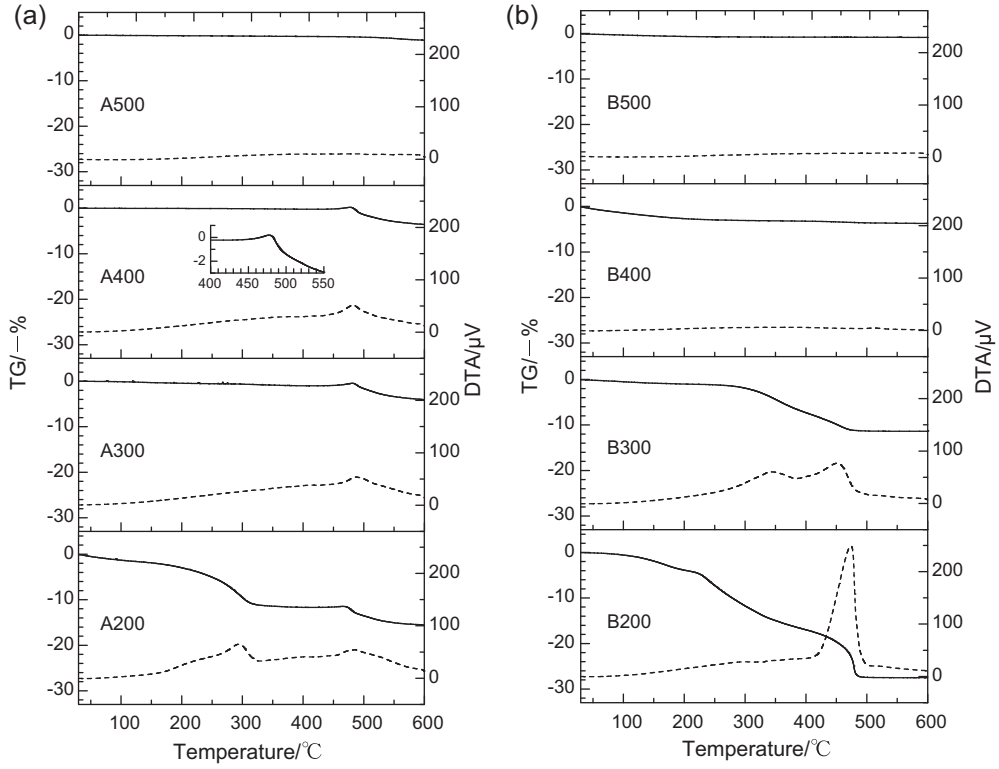

Fig. 14. TG/DTA curves of each samples. (a) A samples, without MEA and (b) B samples, with MEA. The measurements were performed in air atmosphere with a heating rate of 10 °C/min. Solid line: TG, dot line: DTA.

be in melted state at 350 °C and changed into α-PbO cluster as observed by XRD and TEM, therefore, the former peak at around 350 °C can be assigned to the oxidation reaction from Pb^0 to α-PbO. The latter one at around 450 °C was observed simultaneously with the end of weight loss. This is attributed to the pyrolysis of residual metal organic compounds.

For B400, the exothermic peak at around 450 °C was not observed, indicating sufficient heating (1 h) at 400 °C enabled complete decomposition of organics, which is close to the onset of fast decomposition (∼420 °C) in the TG/DTA data of B200 and B300. Note that the real temperature could be slightly lower than the indicated one in a TG measurement. A gradual weight loss below 200 °C was observed for B400, which was considered as evaporation of organic species. B500 has no changes in the TG/DTA curves from room temperature to 600 °C because the pyrolysis had finished during heating at 400 °C for 1 h when the sample was prepared.

As a summary of the present section, in B samples, the addition of MEA induced a rise of the pyrolysis temperature compared with A samples, as well as a suppression of the oxidative reaction until the temperature becomes higher than the melting point of Pb^0.

4. Discussion

The experimental results have revealed that a direct formation of perovskite structure of PZT without passing through pyochlore took place from solution B. It is well known that high temperatures are needed to convert from the metastable pyrochlore phase to the perovskite phase. Thus, skipping pyrochlore phase would greatly accelerate the kinetics of perovskite crystallization because of the avoidance of a high activation energy barrier. This is the reason for our low-temperature crystallization of PZT.

Now, we consider first why pyrochlore was avoided in B samples. There are three necessary conditions for the formation of pyrochlore. The first one is a proper temperature. In general, the formation of pyrochlore structure starts at around 300 °C, though the structure is usually not be well crystallized at such temperature. The second is correct valence states of metals. For PZT, the pyrochlore structure has Pb in divalent and higher valence states. The third is appropriate composition, i.e., a composition that is close to the stoichiometric one, $A_2B_2O_7$. In B samples, both later two conditions were not satisfied. A large amount of Pb was reduced into Pb^0, and separated from the matrix oxides, resulting in a lack of Pb. Therefore, the pyrochlore formation was avoided during the increase of temperature.

The next question is how the structures in solution influenced the formation of Pb^0. EXAFS data of Zr K-edge indicates that the interaction between Zr and Pb in the evaporated samples was destroyed by the coordination of MEA, and aggregation between Zr was dominant. The same phenomenon probably occurred for Ti, which have the common characteristic in group IV, though of which the quality of EXAFS data was not enough for discussion. Meanwhile, Pb was considered to form a single-nuclear complex, and there were hardly Pb–O–Ti/Zr or Pb–O–Pb linkages by the bonding with MEA. Fig. 15 shows the images of local

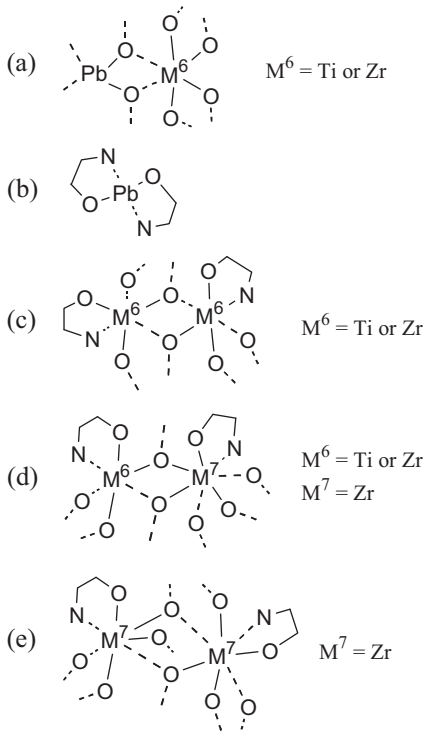

Fig. 15. Expected structures of the metal organic complexes in the solution and evaporated samples. "M^6" represents Ti or Zr atom with 6-fold coordination, whereas "M^7" represents Zr atom with 7-fold coordination. The coordination environments were expected based on XANES data. (a) A samples, without MEA. Heterometallic complexes between Pb and Ti/Zr with 6-fold coordination were expected. (b–e) B samples, with MEA. Pb was separated from Ti/Zr because of MEA coordination. (b) is for the separated Pb complex and (c)–(e) are for Ti/Zr complexes showing that Ti/Zr were in the similar coordination environment with oxide (ZrO_2 and TiO_2) structures in B samples. Not only combinations of the same metals (Ti/Ti or Zr/Zr) but also the ones of different metals (Ti/Zr) are expected, as shown in (c)–(e). (e) indicates a pair of Zr with 7-fold coordination. The Ti–Zr distance could not be detected in EXAFS data, but the existence of Ti–O–Zr connection is expected.[22] Carbon and hydrogen atoms in alkoxide ligands have been omitted.

structure around metals in the solution and evaporated samples. Therefore, the addition of MEA resulted in a separation of Pb from Ti/Zr in the solution. Further, MEA coordination increased thermal stability of the organic components, leading to a higher pyrolysis temperature as observed in the TG/DTA. The rise of pyrolysis temperature and a consequent reducing environment because of the richness in organics enabled the reduction of lead from Pb^{2+} into Pb^0 in the range of 200–300 °C.[17]

At the same time, Zr and Ti formed the amorphous network. Since B200–300 showed large weight losses in these TG/DTA data, MEA must coordinate to Zr/Ti and remained in these stages. A noteworthy fact is, however, that the local arrangements of atoms were nearly the same for both A/B samples heated at 200–400 °C, notably at 300–400 °C, regardless of the presence of MEA. One possibility is that, before complete decomposition of organic components, the amorphous Zr/Ti–O formed a nanograined structure with organic ligands, notably MEA, coordinated to the surface metal atoms of the nanograins. Though the nanograins may grow with the removal of organic ligands, and finally merge into bulk amorphous

Zr/Ti–O, EXAFS data of Zr and Ti K-edge could not distinguish the local Zr–O and Zr–O–Zr or Ti–O and Ti–O–Ti between bulk and such nanograined structure, showing a local environment similar to ZrO_2 and TiO_2. This amorphous matrix acted as a protecting layer of Pb^0 to avoid re-oxidization. These conditions facilitated the separation of Pb^0 and the suppression of pyrochlore.

Pb^0 formed large crystals inside the powder in B300, and converted to homogeneously distributed α-PbO nanocrystals and clusters in B400 (Fig. 6). So, the last question is how the homogeneous distribution of PbO was formed in B400. This can be explained as follows. Pb^0 crystals melted at temperatures (e.g., 400 °C) higher than its melting point, and the Pb liquid could readily diffuse into the surrounding amorphous phase of Zr/Ti–O, and finally was oxidized into α-PbO nanocrystlas and clusters by oxygen coming from air. The diffusion of oxygen through the Zr/Ti–O amorphous phase from air may be slower than the diffusion of Pb over its melting point, resulting in a re-distribution of Pb in the Zr/Ti–O phase. Then, at the perovskite crystallization temperatures (≥400 °C), it is expected that the B samples are crystallized into perovskite structure through solid-state reaction between α-PbO and the amorphous Zr/Ti–O. The uniform distribution of α-PbO in the form of small clusters might have significantly facilitated the reaction. According to a previous study, α-PbO clusters may be an intrinsic precursor for the crystallization of PZT perovskite because of structural relations.[38,39]

In the present study, the reduction (separation) and re-oxidation (re-distribution) of Pb were the key to low-crystallization temperature of perovskite without passing thorough pyrochlore, using a MEA modified PZT solution. We have already reported briefly device-quality PZT films crystallized at 400–450 °C based on the present consideration, where Pb^0 separation was confirmed, but the formation of α-PbO was not observed.[19]

5. Conclusion

We have found a novel crystallization path of PZT without passing through pyrochlore using MEA addition in the chemical solution process. Skipping pyrochlore leads to crystallization of perovskite at low temperatures of 400–500 °C. During temperature increase, the reduction of Pb^{2+} into Pb^0 accompanied by nanoscopic separation of Pb^0 results in deficiency of Pb for the pyrochlore composition $Pb_2(Zr,Ti)_2O_7$. This, together with a reducing environment, is the reason for the avoidance of pyrochlore. Addition of MEA destroys multinuclear Pb–Zr/Ti structures in the solution because of strong coordination of MEA to metal atoms, and also produced organic complexes with a higher decomposition temperature, which, during pyrolysis, provides a reducing environment and produces polycrystalline Pb^0 embedded in the amorphous matrix of Zr/Ti–O, which have the same local structures of ZrO_2 and TiO_2. At elevated temperatures, the polycrystalline Pb^0 is transformed into α-PbO nanocrystals and clusters through diffusion and re-oxidation, gaining a uniform distribution. It is expected that finally, perovskite crystallized through the reaction between α-PbO and amorphous Zr/Ti–O. In the present study, we emphasize that α-PbO clusters might have played an important role as an intrinsic precursor of the perovskite.

Acknowledgments

We thank Professor S. Katayama for helpful discussion and suggestions. TEM observations were conducted in Kyoto-Advanced Nanotechnology Network, supported by "Nanotechnology Network" of the Ministry of Education, Culture, Sports, Science and Technology (MEXT), Japan. This research was supported by Japan Science and Technology Agency.

References

1. Setter N, Damjanovic D, Eng L, Fox G, Gevorgian S, Hong S, et al. Ferroelectric thin films: review of materials, properties, and applications. *J Appl Phys* 2006;**100**:051606.
2. Izyumskaya N, Alivov YI, Cho SJ, Morkoç H, Lee H, Kang YS. Processing, structure, properties, and application of PZT thin films. *Critical Rev Solid State Mater Sci* 2007;**32**:111–202.
3. Bell, Ferroelectrics AJ. The role of ceramic science and engineering. *J Euro Ceram Soc* 2008;**28**:1307–17.
4. Yoshimura M. Soft solution processing: concept and realization of direct fabrication of shaped ceramics (nano-crystals, whiskers, films, and/or patterns) in solutions without post-firing. *J Mater Sci* 2006;**41**:1299–306.
5. Schwartz RW, Schneller T, Waser R. Chemical solution deposition of electronic oxide films. *C R Chim* 2004;**7**:433–61.
6. Tiwari VS, Kumar A, Wadhawan VK, Pandey D. Kinetics of formation of the pyrochlore and perovskite phases in sol–gel derived lead zirconate titanate powder. *J Mater Res* 1998;**13**:2170–3.
7. Bursill LA, Brooks KG. Crystallization of sol gel derived lead zirconate titanate thin films in argon and oxygen atmospheres. *J Appl Phys* 1994;**75**:4501–9.
8. Bao D, Mizutani N, Zhang L, Yao X. Composition gradient optimization and electrical characterization of (Pb, Ca)TiO_3 thin films. *J Appl Phys* 2001;**89**:801–3.
9. Suzuki H, Naoe T, Miyazaki H, Ota T. Deposition of highly oriented lanthanum nickel oxide thin film on silicon wafer by CSD. *J Euro Ceram Soc* 2007;**27**:3769–73.
10. Hwangbo S, Lee Y, Hwang K. Photoluminescence of ZnO layer on commercial glass substrate prepared by sol–gel process. *Ceram Int* 2008;**34**:1237–9.
11. Tanaka H, Tadanaga K, Tohge N, Minami T. Effect of alkanolamines on the microstructure and dielectric properties of lead zirconium titanium trioxide thin films prepared from modified metal alkoxides. *Jpn J Appl Phys* 1995;**34**:L1155.
12. Kim SH, Kim CE, Oh YJ. Preparation of $PbTiO_3$ thin films using an alkoxide–alkanolamine sol–gel system. *J Mater Sci* 1995;**30**:5639–43.
13. Losego MD, Ihlefeld JF, Maria JP. Importance of solution chemistry in preparing sol–gel PZT thin films directly on copper surfaces. *Chem Mater* 2008;**20**:303–7.
14. Faheem Y, Shoaib M. Sol–gel procession and characterization of phase-pure lead zirconate titanate nano-powders. *J Am Ceram Soc* 2006;**89**:2034–7.
15. Martin-Arbella N, Bretos Í, Jiménez R, Calzada ML, Sirera R. Photoactivation of sol–gel precursors for the low-temperature preparation of $PbTiO_3$ ferroelectric thin films. *J Am Ceram Soc* 2011;**92**:396–403.
16. Martin-Arbella N, Bretos Í, Jiménez R, Calzada ML, Sirera R. Metal complexes with N-methyldiethanolamine as new photosensitive precursors for the low-temperature preparation og ferroelectric thin films. *J Mater Chem* 2011;**21**:9051–9.
17. Polli AD, Lange FF. Pyrolysis of $Pb(Zr_{0.5}Ti_{0.5})O_3$ precursors: avoiding lead partitioning. *J Am Ceram Soc* 1995;**78**:3401–4.
18. Chang TI, Wang SC, Liu CP, Lin CF, Huang JL. Thermal behaviors and phase evolution of lead zirconate titanate prepared by sol–gel processing:

the role of the pyrolysis time before calcination. *J Am Ceram Soc* 2008;**91**: 2545–52.
19. Li J, Kameda H, Trinh BNQ, Miyasako T, Tue PT, Tokumitsu E, et al. A low-temperature crystallization path for device-quality ferroelectric films. *Appl Phys Lett* 2010;**97**:102905.
20. Budd KD, Dey SK, Payne DA. Sol–gel processing of $PbTiO_3$, $PbZrO_3$, PZT, and PLZT thin films. *Proc Br Ceram Soc* 1985;**36**:107–21.
21. XAFS analysis software REX2000 version 2.5.9, Manual No.MJ13401A, Rigaku Corporation: Japan.
22. Ankudinov AL, Ravel B, Rehr JJ, Conradson SD. Real-space multiple-scattering calculation and interpretation of X-ray-absorption near-edge structure. *Phys Rev B* 1998;**58**:7565–76.
23. Teff DJ, Huffman JC, Caulton KG. Heterometallic alkoxides of zirconium with tin(II) or lead(II). *Inorg Chem* 1996;**35**:2981–7.
24. Daniele S, Papiernik R, Pfalzgraf LGH. Single-source precursors of lead titanate: synthesis, molecular structure and reactivity of $Pb_2Ti_2(\mu_4\text{-O})(\mu_3\text{-O-}i\text{-Pr})_2(\mu\text{-O-}i\text{-Pr})_4(\text{O-}i\text{-Pr})_4$. *Inorg Chem* 1995;**34**: 628–32.
25. Khanuja M, Kala S, Mehta BR, Sharma H, Shivaprasad SM, Balamurgan B, et al. XPS and AFM studies of monodispersed Pb/PbO core–shell nanostructures. *J Nanosci Nanotechnol* 2007;**7**:2096–100.
26. Mountjoy G, Pickup DM, Anderson R, Wallidge GW, Holland MA, Newport RJ, et al. Changes in the Zr environment in zirconia-silica xerogels with composition and heat treatment as revealed by Zr K-edge XANES and EXAFS. *Phys Chem Chem Phys* 2000;**2**: 2455–60.
27. Peter D, Ertel TS, Bertagnolli H. EXAFS study of zirconium alkoxides as precursor in the sol–gel process: I. Structure investigation of the pure alkoxides. *J Sol–gel Sci Tech* 1994;**3**:91–9.
28. Feth MP, Weber A, Merkle R, Reinöhl U, Bertagnolli H. Investigation of the crystallisation behaviour of lead titanate (PT), lead zirconate (PZ) and lead zirconate titanate (PZT) by EXAFS-spectroscopy and X-ray diffraction. *J Sol–gel Sci Tech* 2003;**27**:193–204.
29. Yamamoto T. What is the origin of pre-edge peaks in K-edge XANES spectra of 3d transition metals: electric dipole or quadrupole? *Adv X-Ray Chem Anal Jpn* 2007;**38**:45–65.
30. Vedrinskii RV, Kraizman VL, Novakovich AA, Demekhin Ph V, Urazhdin SV. Pre-edge fine structure of the 3d atom K X-ray absorption spectra and quantitative atomic structure determinations for ferroelectric perovskite structure crystals. *J Phys Condens Matter* 1998;**10**:9561–80.
31. Babonneau F, Doeuff S, Leaustic A, Sanchez C, Cartier C, Verdaguer M. XANES and EXAFS study of titanium alkoxides. *Inorg Chem* 1988;**27**:3166–72.
32. Camargo ER, Longo E, Leite ER, Mastelaro VR. Phase evolution of lead titanate from its amorphous precursor synthesized by the OPM wet-chemical route. *J Solid State Chem* 2004;**177**:1994–2001.
33. Yu YH, Tyliszczak T, Hitchcock AP. Pb L_3 EXAFS and near-edge studies of lead metal and lead oxides. *J Phys Chem Solids* 1990;**51**:445–51.
34. Sengupta SS, Ma L, Adler DL, Payne DA. Extended X-ray absorption fine structure determination of local structure in sol–gel-derived lead titanate, lead zirconate, and lead zirconate titanate. *J Mater Res* 1995;**10**:1345–8.
35. Moore WJ, Pauling L. The crystal structures of the tetragonal monoxides of lead, tin, palladium, and platinum. *J Am Chem Soc* 1941;**63**:1392–4.
36. Lee JH, Chiang YM. Pyrochlore-perovskite phase transformation in highly homogeneous $(Pb,La)(Zr,Sn,Ti)O_3$ powders. *J Mater Chem* 1999;**9**:3107–11.
37. Chang TI, Huang JL, Lin HP, Wang SC, Lu HH, Wu L, et al. Effect of drying temperature on structure, phase transformation of sol–gel-derived lead zirconate titanate powders. *J Alloys Compd* 2006;**414**:224–9.
38. Bellac DL, Kiat JM, Garnier P, Moudden H, Sciau P, Buffat PA, et al. Mechanism of the incommensurate phase in lead oxide α-PbO. *Phys Rev B* 1995;**52**:13184–94.
39. Pradhan SK, Gateshki M, Niederberger M, Ren Y, Petkov V. $PbZr_{1-x}Ti_xO_3$ by soft synthesis: structural aspects. *Phys Rev B* 2007;**76**:014114.